Journal of Power Sources 381 (2018) 171–180

Contents lists available at ScienceDirect

Journal of Power Sources

journal homepage: www.elsevier.com/locate/jpowsour

Design of high-performance cathode materials with single-phase pathway for sodium ion batteries: A study on P2-$Na_x(Li_yMn_{1-y})O_2$ compounds

Lufeng Yang[a,b], Xiang Li[c], Xuetian Ma[a], Shan Xiong[a], Pan Liu[d], Yuanzhi Tang[d], Shuang Cheng[b], Yan-Yan Hu[c,e], Meilin Liu[b,f,**], Hailong Chen[a,*]

[a] The Woodruff School of Mechanical Engineering, Georgia Institute of Technology, 771 Ferst Drive, Atlanta, GA 30332-0245, USA
[b] New Energy Research Institute, School of Environment and Energy, South China University of Technology, Guangzhou Higher Education Mega Center, Guangzhou, Guangdong 510006, China
[c] Department of Chemistry and Biochemistry, Florida State University, Tallahassee, FL 32306, USA
[d] School of Earth and Atmospheric Sciences, Georgia Institute of Technology, 311 Ferst Drive, Atlanta, GA 30332-0340, USA
[e] National High Magnetic Field Laboratory, 1800 East Paul Dirac Drive, Tallahassee, FL 32310, USA
[f] School of Materials Science and Engineering, Georgia Institute of Technology, 771 Ferst Drive, Atlanta, GA 30332-0245, USA

HIGHLIGHTS

- A group of Mn based cathode materials were synthesized and demonstrated high performance.
- A Solid-solution phase evolution pathway was realized by rational material design.
- Fate of Li in Na-ion cell was revealed by solid state NMR.
- A novel material design strategy for high capacity cathode was raised.

ARTICLE INFO

Keywords:
Lithium excess cathodes
Layered transition metal oxides
Intercalation cathodes
Na ion batteries

ABSTRACT

Sodium-ion batteries (SIBs) are an emerging electrochemical energy storage technology that has high promise for electrical grid level energy storage. High capacity, long cycle life, and low cost cathode materials are very much desired for the development of high performance SIB systems. Sodium manganese oxides with different compositions and crystal structures have attracted much attention because of their high capacity and low cost. Here we report our investigations into a group of promising lithium doped sodium manganese oxide cathode materials with exceptionally high initial capacity of ~223 mAh g^{-1} and excellent capacity retentions, attributed primarily to the absence of phase transformation in a wide potential range of electrochemical cycling, as confirmed by *in-operando* X-ray diffraction (XRD), Rietveld refinement, and high-resolution ^{7}Li solid-state NMR characterizations. The systematic study of structural evolution and the correlation with the electrochemical behavior of the doped cathode materials provides new insights into rational design of high-performance intercalation compounds by tailoring the composition and the crystal structure evolution in electrochemical cycling.

1. Introduction

Sodium-ion batteries (SIBs), as an emerging electrochemical energy storage technology, are advantageous for large scale energy storage because sodium has much higher natural abundance and good availability than lithium [1–3]. Recently, various cathode materials have been intensively investigated for sodium-ion batteries. Among them, layered sodium transition metal oxides, Na_xMO_2 (M = transition metals), promise higher capacities than other types of cathode materials [4–7]. These layered oxides share similar characteristics in crystal structure with the MO_6 edge-sharing octahedra that form parallel slabs, but have subtle difference in the stacking sequence of these slabs. The structural features of the AMO_2 (A = alkaline metal and M = transition metal) oxides are customarily labeled with the notations introduced by Delmas et al. [8], such as P2, O2, O3, and T3, etc., where the letter indicates the coordination environment of the alkaline ion A (prismatic,

* Corresponding author.
** Corresponding author. New Energy Research Institute, School of Environment and Energy, South China University of Technology, Guangzhou Higher Education Mega Center, Guangzhou, Guangdong 510006, China.
E-mail addresses: meilin.liu@mse.gatech.edu (M. Liu), hailong.chen@me.gatech.edu (H. Chen).

https://doi.org/10.1016/j.jpowsour.2017.12.072
Received 8 September 2017; Received in revised form 11 December 2017; Accepted 25 December 2017
Available online 14 February 2018
0378-7753/

octahedral, or tetragonal) and the number indicates the period of stacking of the slabs. In LIB systems, O3-structured cathodes are most commonly used, such as seen in $LiCoO_2$ (LCO) and $Li(NiCoMn)_{1/3}O_2$ (NMC). For SIB cathodes, both P2 and O3 compounds have been intensively studied [5]. Among the P2 and O3 Na_xMO_2 compounds, Mn-based cathode materials attracted most interest due to the low cost of Mn and the interesting intercalation chemistry that is quite different from their lithium counterpart [6,7]. The amount of Na that can be reversibly deintercalate from/intercalate into the structure depends strongly on the structure of the pristine material; while the structure of the pristine materials is also determined subtly by the precursors used and the synthesis conditions. To date, various Na_xMnO_2 materials have been extensively explored, and some of them have displayed good electrochemical performance. Ma et al. [9] have re-investigated O3-$NaMnO_2$ and demonstrated that it can deliver a capacity of 185 mAh g^{-1} at 0.1 C in the voltage window of 2.0–3.8 V, but only 132 mAh g^{-1} capacity remains after 20 cycles. Billaud et al. [10] have reported that β-$NaMnO_2$ exhibited a high capacity (of ~190 mAh g^{-1} at 0.1 C in the voltage range of 1.5–4.7 V) and complex structural change that resulted in the collapse of the long-range structure at low Na content, thus compromising the reversibility of the Na extraction and insertion processes. Morales et al. [11] reported that layered P2-$Na_{0.6}MnO_2$ can deliver an initial discharge capacity of 150 mAh g^{-1}. However, this cathode material displayed more than 50% capacity loss after 10 cycles due to the structural degradation and amorphization of the active materials upon successive cycling.

In O3-structured cathodes, Na ions sit at the octahedral sites in the alkaline metal layer. Due to the large size of Na^+, when they are gradually extracted from the alkaline metal layer, the neighboring MO_2 slabs tend to slide coordinately to accommodate the change in the inter-slab distance and reduce the energy of the structure [6]. Such coordinated sliding causes phase transitions. It is commonly seen that Na-O3 compounds experience more phase transitions induced by the slab sliding than Li O3 compounds do [12–14]. The frequent occurring sliding of the slabs introduces dislocations substantially lowers the long-term cyclability of the electrode. On the other hand, it seems Na_xMO_2 compounds with P2 structures show less phase transition in cycling and therefore offer better capacity retention. A high capacity P2 compound $Na_{2/3}(Fe_{1/2}Mn_{1/2})O_2$ exhibits 190 mAh g^{-1} capacity in the first cycle with only a phase transition from P2 to OP4 at high voltage [15]. Another P2 compound, P2-$Na_{2/3}(Mn_{1/2}Fe_{1/4}Co_{1/4})O_2$ that shows high rate capability, was also considered to benefit from less phase transitions [16]. Though superior in capacity to O3 compounds, P2 compounds display only fair cycling performance, likely due to their irreversible phase transitions and large volume change during Na-ions de/intercalation processes [11,17–19]. Efforts have been attempted to mitigate the phase transitions and improve the cyclability of P2 compounds with proper doping. Much work has been done on doping in the transition metal (TM) layer with mixed TM ions, including binary, ternary, and even quaternary mixing of TM ions [19–24]. For instance, Meng et al. demonstrated that good cyclability and rate capability can be achieved by eliminating the P2-O2 transition in P2-$Na_{0.78}(Ni_{0.23}Mn_{0.69})O_2$ [24]. Doping in the TM layer with redox non-active elements, such as Li [25–28], Mg [29–31] and Zn [22] represents another approach. This type of doping increases the stability of the structure, resulting in improved capacity retention but reduced theoretical capacity. Billaud et al. have explored Mg-doping in P2-$Na_{0.67}(Mn_{1-x}Mg_x)O_2$ and shown that substitution of a small amount of Mn (x = 5%) with Mg could effectively enhance the overall performance without sacrificing much on the capacity [29]. Guo et al. also demonstrated that suppressing the P2-O2 transition by magnesium substitution is beneficial for the performance and cycle life of $Na_{0.67}Mn_{0.67}Ni_{0.33}O_2$ compounds [31]. Besides TM mixing and Mg doping, some efforts have also demonstrated that Li-substitution at the TM sites is also beneficial for the performance [26–28,32,33]. Kim et al. reported improved cycling stability of P2-$Na_{1.0}Li_{0.2}Ni_{0.25}Mn_{0.75}O_{2+d}$ [27]. This material exhibited a specific capacity of 95–100 mAh g^{-1} between 2.0 and 4.2 V, along with good cycling and rate capabilities. Meng et al. [32] investigated the mobility of Li-ions in $Na_{0.8}Li_{0.12}Ni_{0.22}Mn_{0.66}O_2$ compound during the first cycle of charge and discharge. This compound displayed an initial discharge capacity of 133 mAh g^{-1}. Komaba et al. have reported that $Na_{5/6}[Li_{1/4}Mn_{3/4}]O_2$ compound displays ~200 mAh g^{-1} of reversible capacity between of 1.5 and 4.4 V at a rate of 10 mA g^{-1} [26]. Part of the capacity of this compound is suggested to be due to oxygen evolution. Recently, $Na_{0.6}Li_{0.2}Mn_{0.8}O_2$ were synthesized by self-combustion reactions and shown that it exhibits good capacity of 190 mA h^{-1} between 2.0 and 4.6 V at C/15 [33] and interesting activation process during cycling.

Previous studies, as surveyed above, demonstrated that Li-substitution at the TM site is beneficial to the capacity and cycle life. However, the fundamental mechanism for this performance enhancement remains to be better understood, e.g. what role does Li play in the structure and how it changes the stability of the P2 and O3 phases; What is the fate of Li in long-term cycling and how does it impact the structural evolution of the electrode materials after long-term cycles, etc. Here we report our findings in systematic investigations into a group of Li-doped P2-structured model compounds and the new design strategies towards high capacity, long cycle life cathodes for SIBs. $Na_{0.6}Li_{0.2}Mn_{0.8}O_2$ was designed as the primary model compound and other compositions, including $Na_{0.7}Li_{0.23}Mn_{0.77}O_2$, $Na_{0.75}Li_{0.25}Mn_{0.75}O_2$, and $Na_{0.8}Li_{0.27}Mn_{0.73}O_2$, were also synthesized via a solid-state reaction and tested as cathode materials in sodium half-cells. The major motivation of using lithium as the doping elements, instead of Mg or Zn, is not only based on the good performances previously reported. Our hypothesis is that the local ordering or clustering of Li and Mn in the TM layer may effectively lock the coordinating oxygen atoms and increase the activation energy for their gliding, so as to hinder or delay the phase transitions. For this purpose, lithium is a better choice than most of other metals as the clustering effect between Li^+ and Mn^{4+} is more pronounced than those between 2 + or 3 + metals and Mn^{4+}. In addition, the light lithium atom as dopant does not reduce the theoretical capacity as much as other redox non-active metals, such Mg or Zn. P2 structure was chosen as the base structure for optimization not only because more P2 compounds were reported to have superior performances than O3 compounds. More importantly, in P2 structure, lithium is expected to be accurately doped into Mn sites in the TM layers because the prismatic sites in the alkaline metal layer is strongly unfavorable for Li^+. In this way, we can have a group of model compounds with rather well controlled crystallographic sites and ordering status, which would facilitate the extraction of new insightful information from systematical experiments. Electrochemical testing and *in operando* X-ray diffraction (XRD) were used to follow the phase evolutions of the model compounds and to directly correlate the structural features with the electrochemical behavior. Solid-state ^7Li NMR was combined with *in operando* XRD to detect the crystallographic sites of lithium and to reveal their fate in successive electrochemical cycles.

2. Experimental section

2.1. Materials preparation

The P2-$Na_x(Li_yMn_{1-y})O_2$ compounds (x = 0.6, 0.7, 0.75, 0.85; y = 0.2, 0.23, 0.25, 0.27) were synthesized by solid-state reaction from starting materials of sodium carbonate (Na_2CO_3, Alfa, 99.7%), lithium carbonate (Li_2CO_3, Alfa, 99.7%), and manganese oxide (MnO_2, Alfa, 99.7%) with stoichiometric ratios. Lithium and sodium sources were used in 5% excess to compensate their loss in high temperature calcination. The starting materials were mixed in a stoichiometric ratio and ground with using a planetary high-energy ball milling [Retsch PM200] at 300 rpm for one hour. The mixture was then pressed into pellets and calcined in air at 800 °C for 12 h with a ramping rate of 5 °C per minute.

After heating, the pellets were quenched to room temperature by quickly placing them on a copper plate. The quenched pellets were then transferred to an Ar-filled glovebox immediately to minimize contact with air and moisture.

2.2. Electrochemical testing

P2-$Na_x(Li_yMn_{1-y})O_2$ active material and carbon black (Timcal, super P) were first mixed in a Retsch PM200 planetary ball mill at 300 rpm for one hour to achieve a good mixing and a carbon coating on the surface of the active material particle. Positive electrodes were then prepared by mixing the carbon coated active material (80 wt%) with additional carbon black (10 wt%, Super C65, TIMCAL) and polivinylidenedifluoride (PVdF, 10 wt%, 6020 Solef, Arkema Group). The slurry was made by adding an appropriate amount of N-methyl-2-pyrrolidone (NMP). After thoroughly hand mixing, the slurry was cast onto an aluminum foil and dried at 100 °C in a vacuum oven overnight. The dried film was roller-pressed and cut into round disks of 15 mm diameter. Sodium metal foil was used as the negative electrodes. The electrolyte solution used was $NaPF_6$ (1 mol) dissolved in propylene carbonate (PC). A piece of glass fiber filter GF/D (Whatman) was used as the separator. CR2016-type coin cells were then assembled in an Ar-filled glovebox and tested with an Arbin battery cycler (BT2043).

2.3. Materials characterization

X-ray diffraction (XRD) pattern were first collected with using a Bruker D8 Advance diffractometer equipped with a molybdenum target. Patterns of Mo Kα radiation in the 2θ range from 6° to 40° were used to determinate the crystalline structure of the samples. The crystalline structure of the sample was further investigated using synchrotron radiation source at the XPD beam line at the National Synchrotron Light Source II (NSLS-II) at Brookhaven National Laboratory (BNL). All the samples were well sealed with Kapton film to avoid air exposure during the test. Later, selected samples were also tested with using synchrotron radiation source at beam line 17-BM at the Advanced Photon Source (APS) at the Argonne National Laboratory (ANL). *In situ* XRD for the solid-state synthesis process was performed with using a HTK1200N temperature chamber installed on a Bruker D8 Advanced diffractometer. The pellet sample was heat in the chamber with using a program shown in Fig. S1. At each designed temperature, XRD pattern was collected while the temperature was held constant with accuracy of ± 1 °C. Morphological investigation of the samples was conducted using Field-Emission Scanning Electron Microscopy (FE-SEM, Hitachi LEO 1530). *In operando* XRD of the samples were first performed on the Bruker D8 with an *in situ* battery cell in reflection mode. The *in situ* cell was charged/discharged within a voltage domain of 1.5–4.5 V at a rate of C/30. Each scan covered 2-theta range of 6°–40° in a time duration of two hours. *In operando* SXRD on selected samples were also performed using synchrotron radiation source at beam line 17-BM at APS with using an *in situ* battery cell in transmission mode. The patterns were collected every 5 min.

3. Results

3.1. Synthesis and in situ XRD for synthesis

In the first a few attempts of solid state synthesis of the model compound $Na_{0.6}Li_{0.2}Mn_{0.8}O_2$, a P2 phase was successfully obtained by heating the pellets at 800 °C with the presence of minor impurities. To further purify the phase and determine the best synthesis condition, *in situ* XRD for synthesis was performed using a HTK1200N temperature chamber installed on a Bruker D8 Advanced diffractometer. The pellet sample was heated in the chamber using a program shown in Fig. S1. At each designed temperature, XRD pattern was collected while the temperature was held with accuracy of ± 1 °C. The XRD patterns in the whole heating-cooling process are shown in Fig. 1. It can be seen that the sharp and strong peaks of MnO_2 from starting materials gradually disappear starting at 350 °C and a new phase starts to form at the same time with characteristic peaks at 8.7 and 17.3°. This phase is likely to be an O3 phase majorly containing lithium, as the characteristic peak around 8.7° and 17.3° are very close to the (003) and (104) peaks for many lithium O3 compounds. At 500 °C, a sodium O3 phase is formed, evidence from the (003) peak at 7.4°, which corresponds to a large d-spacing in *c*-axis for sodium O3 compounds. Soon after, the Li and Na O3 phases react to form an O3 phase likely with both Li and Na in the alkaline metal layer. Since the ratio of Na: Li in the starting materials is 0.6: 0.2, the d-spacing of the Li-Na mixed O3 phase is more close to that of the Na O3 phase, evidence from the position of the (003) peak. Staring at 650 °C and finishing at 700 °C, the Li-Na O3 phase transforms to a P2 phase, which is likely our target phase of P2-$Na_{0.6}Li_{0.2}Mn_{0.8}O_2$. When temperature is further increased to 950 °C, another phase transformation occurs and an unidentified new phase appears. In the following cooling steps, however, when temperature drops from 1050 °C to 800 °C, the P2 phase appears again as the major phase with minor peaks from the high temperature new phase. It is difficult to solve this high temperature phase using the *in situ* XRD. However, from the pattern and the fact that it can very quickly convert to P2 phase in cooling in only a few minutes, we speculate that this phase is a completed disordered phase with an O3-like framework and randomly distributed alkaline and TMs, inducted by the thermal fluctuations at the high temperature. We have attempted to quench the sample from 1050 °C to identify this phase. Complicated mixture of 3 or 4 phase, including this unknown phase and the P2 phase, was obtained and its electrochemical performance was very low. We speculate that the disordered phase should be avoided in the synthesis. We also compared the electrochemical performance of the samples with pure P2 phase by direct heating at 800 °C and by heating first to 1050 °C then slow cooling to 800 °C. The former sample showed much better performances, again indicating that the high temperature (above 950 °C) phase transitions should be avoided. Therefore, we concluded that the best synthesis condition for the P2 phase is to keep the synthesis temperature below 950 °C. In all below presented characterization and electrochemical testing, samples were synthesized with using heating at 800 °C for 12 h followed by quenching.

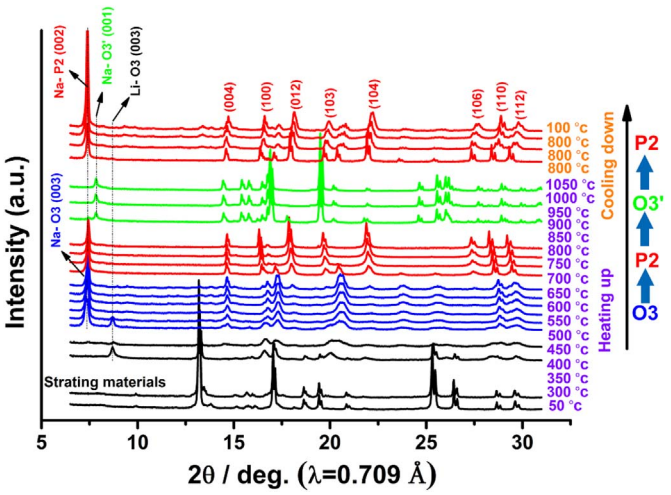

Fig. 1. In situ XRD for sample synthesis via a HTK1200N temperature chamber. The temperature was first set to 50 °C and 300 °C and held for 1 h, then the temperature was increased from 300 °C to 1050 °C with a step of 50 °C and held for 1 h at each temperature, subsequently the temperature was cooled down to 800 °C and held for 3 h and finally cooled down to 100 °C and held for 1 h. The heating rates were 29 °C/min and − 29 °C/min for the heating and cooling process, respectively. XRD patterns were acquired at each temperature after it was stabilized for 1 h.

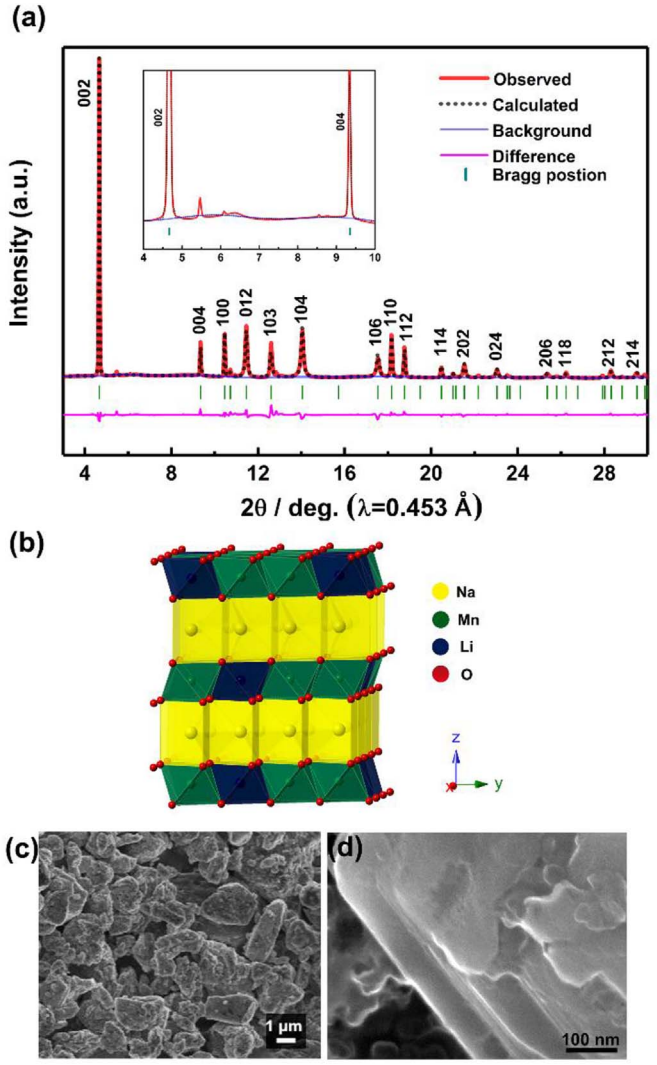

Fig. 2. (a) Rietveld refinement (red line) of $Na_{0.6}Li_{0.2}Mn_{0.8}O_2$ in the space group of $P6_3/mmc$ (black dots marks) using SXRD pattern (λ = 0.453 Å, red line). The difference between calculated and observed patterns is shown in magenta line, (b) A schematic illustration of the refined P2-type layered structure, (c) SEM image of the as-prepared primary sample and (d) SEM image of the sample after carbon coating by ball mill. (For interpretation of the references to colour in this figure legend, the reader is referred to the Web version of this article.)

3.2. Material characterization

The as-synthesized P2-$Na_{0.6}Li_{0.2}Mn_{0.8}O_2$ sample was characterized using synchrotron X-ray diffraction (SXRD) and scanning electron microscopy (SEM) shown in Fig. 2. The SXRD patterns of P2-$Na_{0.6}Li_{0.2}Mn_{0.8}O_2$ are shown in Fig. 1a and Fig. S2. All reflections can be indexed to a hexagonal lattice with a space group of $P6_3/mmc$ (JCPDS: 54-0894), except for a very low intensity peak at 5.46°, as shown in the inset of Fig. 2. We speculate it to be a trace impurity of $LiMn_2O_4$ phase. The even lower diffraction peaks at 6.0° shown in the inset can be assigned to the "1/3 1/3 0" superlattice, a commonly seen Li^+/Mn^{4+} in plane ordering with a $\sqrt{3}a \times \sqrt{3}a$ -type supercell in Li_2MnO_3 and Li-excess cathode materials [26,34]. Rietveld refinement of the SXRD pattern was implemented with using the GSAS + EXPGUI suite [35,36]. Fig. 2b shows the structural model of this compound. As discussed in the introduction, it is expected that Na takes the prismatic site in the alkaline metal layer, while lithium prefers to take the smaller octahedral site in the TM layer. Li-Na mixing in the alkaline metal layer is not preferred due to high energy penalty. With using this structural model, the lattice parameters are refined to be $a = b = 2.870(8)$ Å and $c = 11.125(6)$ Å. The cell volume V = 79.409(5) Å^3 with good goodness of fit wRp (10.0%). The detailed refinement results are listed in Table S1. It is noted that anisotropic peak broadening is observed for (10l) reflections. Similar anisotropic broadening was also observed in P2 compounds such as $Na_{2/3}[Fe_{1/2}Mn_{1/2}]O_2$ [15] and $Na_{5/6}[Li_{1/4}Mn_{3/4}]O_2$ [26]. We speculated that this peak broadening may be due to stacking faults of P2 structure or similar defects resulted from the synthesis. The SEM images show that the primary particles have an average size of 2–5 μm (Fig. 2c) along with well-crystallized solid shapes with hexagonal features (Fig. 2d).

3.3. Electrochemical properties

Electrochemical performance of the $Na_{0.6}Li_{0.2}Mn_{0.8}O_2$ sample was evaluated in CR2016 coin cells with Na metal foil as the anode. Fig. 3b and c shows the voltage profiles and the cycling performance of the cells at a current density of 29.4 mA g^{-1} between 1.5 and 4.5 V. Similar to what was reported in the references [24,25] for P2 sodium manganese oxides and Li-excess lithium cathode materials in LIBs [37], the first charging curve show a long plateau at high voltage, which is likely due to both the electrolyte decomposition and the evolution of oxygen. Because in the pristine material all Mn is in +4 and less likely the Mn^{4+}/Mn^{5+} redox is active. In the following cycles, P2-$Na_{0.6}Li_{0.2}Mn_{0.8}O_2$ exhibited smooth slopping curves for both charge and discharge, suggesting that sodium extraction/insertion proceeds via a solid solution pathway, which was similar to other previous reported P2 compounds, such as $Na_{0.8}[Li_{0.12}Ni_{0.22}Mn_{0.66}]O_2$ reported by Xu et al. [32], and $Na_{2/3}[Mg_{0.28}Mn_{0.72}]O_2$ reported by Naoaki Yabuuchi [38]. The discharge capacity of the first cycle is ~223 mAh g^{-1} (~0.76 Na^+ per formula unit), which is 95% of the theoretical capacity of the materials calculated based on the redox of Mn^{3+}/Mn^{4+}. Though the cell experienced a capacity drop to ~198 mAh g^{-1} at the second cycle, a fairly high discharge capacity of 153 mAh g^{-1} remained after 50 cycles. More than 77% of the reversible capacity was retained after 50 cycles

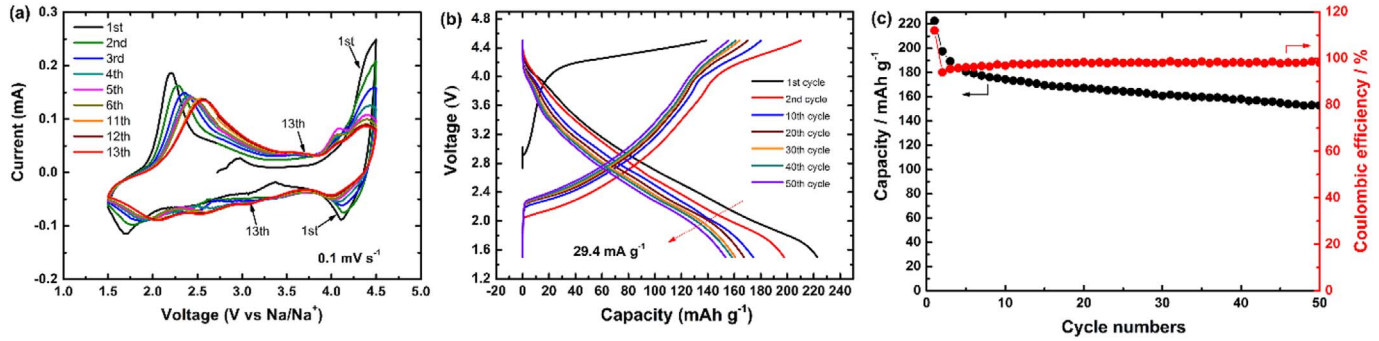

Fig. 3. Electrochemical performance of Na/PC, $NaPF_6$ 1M/$Na_{0.6}Li_{0.2}Mn_{0.8}O_2$ cell cycled within the 4.5–1.5 V (vs Na/Na^+) voltage window. (a) Cyclic voltammogram curves collected at a scan rate of 0.1 mV s^{-1}; (b) galvanostatic charge-discharge cycles at a rate of 29.4 mA g^{-1}; (C) Discharge capacity and coulombic efficiency of the cell as a funtion of the cycle numbers.

when compared with the value of the second cycle and the average capacity retention rate per cycle is calculated to be as high as 99.5%. The high capacity and, particularly, the high capacity retention demonstrated that P2-$Na_{0.6}Li_{0.2}Mn_{0.8}O_2$ could be a promising cathode mateials for sodium-ion battery. To futher understand the cycling process, cyclic voltammetry (CV) scan of the $Na_{0.6}Li_{0.2}Mn_{0.8}O_2$ electrode was performed and the data is shown in Fig. 3a. A high anodic peak appears in the first charge above 4.0 V, corresponding to the combination of oxygen evolution and possible electrolyte decomposition. This peak becomes significantly lower in following cycles while the other anodic peaks centered at 2.5 V are still pronounced. This may imply that the major contribution of this anodic peak at high voltage is majorly caused by oxygen evolution, not electrolyte decomposition, as otherwise it should not decrease as long as there is sufficient electrolyte to keep the cell running or a good SEI is formed. At voltages above 4.2 V, where the compounds retain a small quantity of Na ions, the strong cathodic peak may be attributed to the reversible oxygen evolution through the formation and decomposition of peroxide/superoxide-like species, as claimed in $Na_{0.78}(Ni_{0.23}Mn_{0.69})O_2$ [24] and other similar compounds [39–41]. The 2.5 V anodic peak is attributed to Mn^{3+}/Mn^{4+} redox and the shifting of its center is likely due to the structural change caused by oxygen evolution and other accompanying structural reorganization of the lattice [42]. In successive cyclic scans, the position and intensity of the peaks repeat themselves very well upon cycling, indicating a good reversibility of the structure after the possible structural rearrangement and relaxation to accommodate the oxygen loss in the initial a few cycles.

$Na_x(Li_yMn_{1-y})O_2$ samples with different doping level of lithium were also designed, synthesized and electrochemically tested. The content of Li is increased from 0.2 in the model compound $Na_{0.6}Li_{0.2}Mn_{0.8}O_2$ and the content of Na and Mn (+4) was adjusted to keep the charge neutrality. Theoretically, the upper limit of doping Li into the TM layer in the layered dioxides should be y = 0.33, i.e. $NaLi_{0.33}Mn_{0.66}O_2$, which resembles Li_2MnO_3. However, $NaLi_{0.33}Mn_{0.66}O_2$ may prefer to form an O3 structure, not P2, as P2 structure favors Na contents of ~0.4–0.85 [6,32]. Samples with y = 0.23, 0.25 and 0.27 have been attempted for synthesis following the same synthesis condition. Their XRD patterns are shown in Fig. S3. The composition of y = 0.25 seems to be the upper limit of lithium doping that allows the formation of a single P2 phase, as in the y = 0.27 sample, minor impurity of O3 phase can be detected, evident from the peaks around 17° and 20°. More pronounced superstructure peaks are also observed for sample with y > 0.2. Fig. 4a and b shows the first two cycles of charge-discharge profiles of $Na_x(Li_yMn_{1-y})O_2$ samples and Fig. 4c and d shows the cycling capacity of samples with y = 0.23 and 0.27. Similar to P2-$Na_{0.6}Li_{0.2}Mn_{0.8}O_2$, all the samples show very high initial discharge capacities > 190 mAh g^{-1}, while the capacity retention is worse than that of $Na_{0.6}Li_{0.2}Mn_{0.8}O_2$. The lower long term cycling capacities may not only because of less redox active Mn in the formula. More importantly, it may be due to a more significant rearrangement of the structure caused by oxygen evolution in the initial cycles.

3.4. Single-phase pathway in electrochemical cycling

To further understand the cycling mechanisms of P2-type $Na_{0.6}Li_{0.2}Mn_{0.8}O_2$, the structural evolution during the initial and second galvanostatic cycle was investigated by *in operando* XRD. The patterns are shown in Fig. 5. Selected ranges of the XRD patterns are displayed along with the pattern of the pristine electrode material at the bottom, and the voltage profile on the right. The *in operando* scan was set to start with the cell in resting with an open circuit potential (OCP) of ~2.80 V, followed by a C/30 rate constant current (CC) charging to 4.5 V, then a constant voltage charging at 4.5 V for 2 h, and a C/30 CC discharging to 1.5 V. The second cycle was performed with the same rate but without the constant voltage charging step. Each XRD scan took two hours. As a result, $Na_{0.6}Li_{0.2}Mn_{0.8}O_2$ was capable of delivering high discharge capacity of ~208 mAh g^{-1} (0.71 Na^+ per formula) and ~215 mAh g^{-1} (0.73 Na^+ per formula) in the first and the second cycle, respectively, which are very close to what are obtained from the coin cells. These high capacities imply that the *in operando* XRD can well represent the electrochemical processes taking place in the real cycling condition in coin cells.

In the first cycle, upon charging, both (002) and (004) diffraction peaks, corresponding to the inter-slab distances in *c*-axis, slightly shift to lower two-theta before the potential reaches 4.2 V, indicating an expansion of the unit cell along *c* direction. On the other hand, (100), (102) and (103) diffraction peaks progressively move towards higher two-theta angle, indicating a shrinkage in *a-b* plane due to the decrease in electrostatic repulsion among the Na^+ ions. The (002) and (004) peaks slightly shift back to higher two-theta values as the voltage increase from 4.2 V to 4.5 V, indicating a shrinking along *c* direction as too much sodium ions have been extracted from the alkaline layer. In discharge, the shifting trend reverses from what is observed in charge. But at the end of discharge, (002) and (004) peaks shift to two-theta angles that are higher than those in the pristine film. This agrees well with the sodium content at these states: the pristine samples contain 0.6 Na per formula unit, while after a 208 mAh g^{-1} (~0.71 Na) discharging, the sample at the end of discharge should at least have a Na content higher than 0.71, though the Na content at the end of discharge can not be accurately quantified by coulombs counting owing to the unknown capacity contribution from oxygen evolution and electrolyte decomposition. In the second cycle, the trend of peak shifting largely repeat what is observed in the first cycle but different in two aspects. First is that peak shifting to low two-theta angle is more pronounced than that in the first cycle. That is because in the first charging, the major capacity is contributed from oxygen reduction and involve less Na^+ extraction; while in the second charging, the vast majority part of the capacity is from Mn^{3+}/Mn^{4+} oxidation associate with the removal of Na^+, which apparently varies the cell parameters more significantly. Second is the appearance of a weak peak at ~8.7° at high voltage, which can not be indexed with known phases or superlattices. It does not belong to any O2 phases that are commonly observed at the end of charge states of P2 compounds as this d-spacing of this peak is ~4.2 Å, which is much lower than those of (002) peaks of O2 phases (commonly ~4.4 Å).

It is worth noting that in the first and second cycles, though the redox reactions are different in charging, the crystal structure is well kept in a P2 frame. No obvious O2 phase or other new phases are observed. A solid solution pathway is taken within the full range of charge-discharge cycle, which is in agreement with the slopping voltage profile. This observation is also confirmed with high resolution synchrotron XRD. The synchrotron *in operando* XRD patterns are included in Fig. S4 in the supplementary information. Further, the variation of lattice parameters during the second cycle are extracted with refinement on each pattern and presented in Fig. 6 and Fig. S5, respectively. Fig. 6 shows the evolution of *a* and *c* lattice parameters of the P2-$Na_{0.6}Li_{0.2}Mn_{0.8}O_2$ electrode during the second charge/discharge process. In charging, a gradually decreases and *c* increases and the trends reverse in discharging. The variation of both *a* and *c* is very reversible, indicating a high stability of the P2 structure and excellent reversibility upon Na insertion/extraction in a significantly wide range of > 0.73 Na per formula unit. This range of Na intercalation/deintercalation of 0.73 Na per formula unit is far beyond what is observed in commercial O3-$LiMO_2$ compounds, where usually only 0.5–0.6 Li per formula can be reversibly intercalated, and what is reported from most P2 and O3 sodium cathodes.

3.5. Structural stability upon long-term cycling

From the *in operando* XRD results of the first two cycles, it is clear that the P2 structure is rather stable against Na insertion and extraction in a very large range of sodium fraction. To further detect the stability

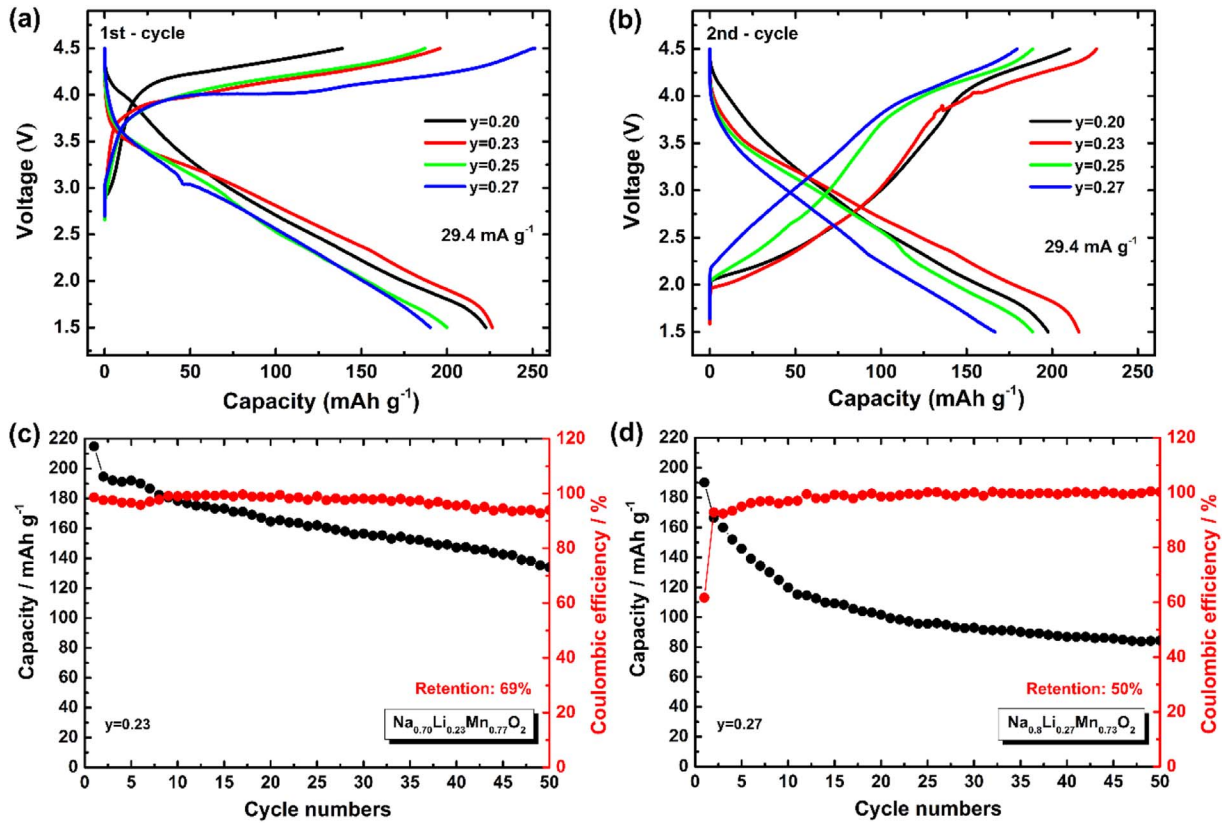

Fig. 4. Electrochemical performance of the $Na_x(Li_yMn_{1-y})O_2$ samples ($Na_{0.6}Li_{0.2}Mn_{0.8}O_2$, $Na_{0.7}Li_{0.23}Mn_{0.77}O_2$, $Na_{0.75}Li_{0.25}Mn_{0.75}O_2$ and $Na_{0.8}Li_{0.27}Mn_{0.73}O_2$) within the 4.5–1.5 V (vs Na/Na^+) voltage window. Galvanostatic charge-discharge cycles of the four samples: (a) first cycle, (b) second cycle. Discharge capacity and coulombic efficiency of the cells as a funtion of the cycle numbers: (c) $Na_{0.7}Li_{0.23}Mn_{0.77}O_2$, (d) $Na_{0.8}Li_{0.27}Mn_{0.73}O_2$.

of the P2 structure in long term cycling, *ex situ* SXRD on a film after 100 cycles was conducted and compared with the SXRD pattern of the pristine powder, as shown in Fig. 7. The pattern of the sample after 100 cycles is almost identical to that of the pristine powder in peak positions. Yet some peak broadening was observed in most peaks, implying a poorer crystallinity or smaller particle size of the cycled sample than those of the pristine. In addition, *in operando* XRD on a film in the 51th cycle was conducted with using synchrotron radiation to explore whether there is any change in phase evolution pathway in long term. The film had been cycled in an *in situ* cell for 50 cycles prior to the XRD scans. The patterns are shown in Fig. S6 in the supplementary information. The trend of peak shifting is the same as what is observed in the second cycle, indicating the single-phase evolution pathway of the P2 framework still dominates after 50 cycles of Na extraction/insertion. Such a highly repeatability of the *in-operando* SXRD result for a long-term cycled electrode suggests that the electrode materials have an extremely stable structure against Na insertion and extraction, implying a high promise of achieve a long cycling life sodium battery system based on this cathode material. Additionally, the SEM images in Fig. S7 in the supplementary information show that the (100 full cycles) cycled electrode materials still retain a hexagonal morphology. The particle size is slightly smaller than that of the pristine sample, which may be caused by the cyclic volume change in cycling and therefore induced cracks in the big particles. Nevertheless, the highly structural stability of electrode materials is key for P2-$Na_{0.6}Li_{0.2}Mn_{0.8}O_2$ to deliver a high capacity retention of 77% with a high initial capacity of more than 200 mAh g^{-1}.

While the P2 structure is well preserved in long term cycling, it is worth to detect the fate of lithium in cycling as lithium can be involved in the intercalation/deintercalation reaction, given the similarity between Li and Na ions. Since X-ray is not sensitive to small site-occupancy changes of light atoms such as Li, we used solid-state ^{7}Li NMR as a tool to examine the local structural environment of Li ions in both pristine and electrochemically cycled $Na_xLi_yMn_{1-y}O_2$ samples. Solid-state ^{7}Li NMR is very powerful to differentiate various local environments of lithium in both crystalline and amorphous solids as previously being demonstrated by Grey et al. in its applications on electrode materials for lithium ion batteries [43–45]. ^{7}Li pj-MATPASS NMR was conducted using a Bruker 2.5 mm magic-angle-spinning (MAS) probe on a AVANCE III spectrometer in a 11.7 T magnet and the sample was spun at 25 kHz. Fig. 8a shows the ^{7}Li pj-MATPASS spectrum of the $Na_{0.6}Li_{0.2}Mn_{0.8}O_2$ pristine powder. Three resonances were observed at 750, 1550 and 2100 ppm, respectively. According to the assignment of ^{7}Li resonances in previous literature on Li_2MnO_3 and other layered oxide materials, we attribute the 750-ppm resonance to be the lithium sitting in the alkaline layer and the 1500 ppm resonance to be lithium in the TM layer. However, for the broad resonance centered around 2100 ppm, was not previously observed in the ^{7}Li spectra of layered oxide materials. Given that in the P2 structure the Li-O-Mn bond angle for lithium in the TM layer is slightly different from that in the O3 structure, it is possible that the electron spin density transfer from Mn can result in a more positive shift per Li-O-Mn contact. Therefore, we tentatively assign the 2100-ppm resonance also as lithium in the TM layer, but in more distorted coordination environments. The large breadth of the 2100-ppm resonance suggests a broad distribution of Li local coordination. Small Li ions can often be accommodated in various structural sites in open structures of layered oxides established with relatively large Na ions. The differences between the lithium of the 2100 and the 1500 ppm resonances may be due to their different environment in the neighboring alkaline layer, e.g. if the closest prismatic sites in the neighboring alkaline layer are taken by Na or not (noting that with only 0.6 Na per formula in this sample, only 30% of the available prismatic sites are occupied by Na). Quantification based on the area integral of the three NMR resonances indicates that about 9%

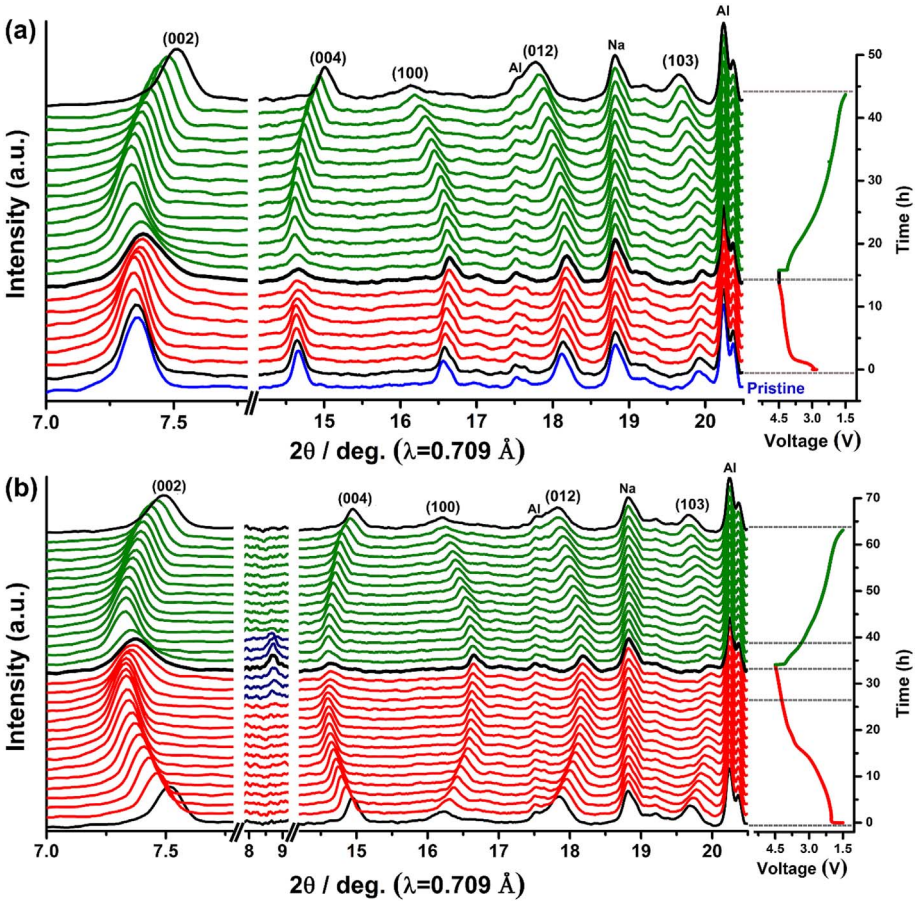

Fig. 5. *In operando* XRD patterns collected during the first two cycles of charge/discharge process of the $Na_{0.6}Li_{0.2}Mn_{0.8}O_2$ electrode, cycled between 1.5 and 4.5 V and remained at 4.5 V for 2 h at a current rate of 1/30 C (7.83 mA g^{-1}): (a) first cycle, (b) second cycle.

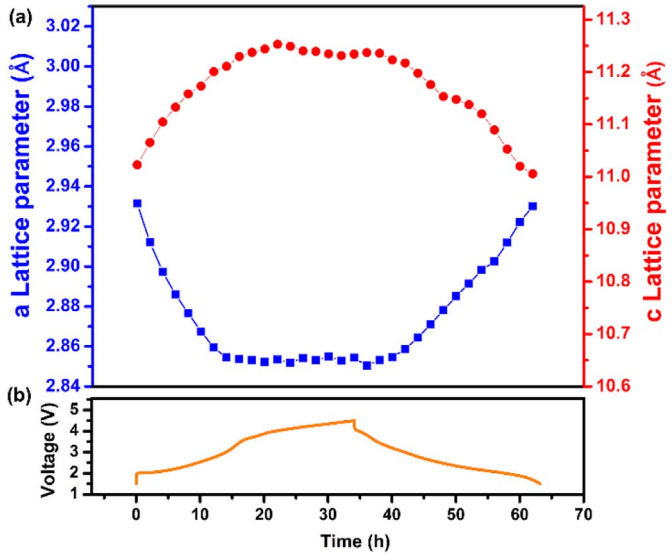

Fig. 6. Evolution of *a* and *c* lattice parameters of the P2-$Na_{0.6}Li_{0.2}Mn_{0.8}O_2$ electrode during the second charge/discharge cycle, obtained by fitting the XRD patterns in Fig. 5.

of Li sits in the alkaline layer and 91% of Li sits in the TM layer. Such distribution of lithium is desired and expected from our design principles. The fate of these Li ions in $Na_{0.6}Li_{0.2}Mn_{0.8}O_2$ electrode upon electrochemical cycling was probed by performing ^{7}Li pj-MATPASS NMR on samples charged to 4.2 V, 4.5 V and discharged after 10 and 40 charge-discharge cycles, respectively. The three previously observed resonances remain but with different relative intensities. In addition, a sharp new resonance at 0 ppm is observed. This resonance is assigned to diamagnetic lithium-containing species, such as Li_2CO_3 or LiF, which are commonly seen as the components of the solid electrolyte interphase (SEI) layer in Li-ion batteries. In this Na-ion battery cell, the electrolyte is $NaPF_6$/PC, which is essentially similar to the electrolyte of Li-ion batteries. Therefore, it is not a surprise to see the formation the Li-SEI-like phases.

The quantification of Li with using the ^{7}Li NMR spectra of the pristine and cycled $Na_{0.6}Li_{0.2}Mn_{0.8}O_2$ indicates significant changes in both the distribution and the total amount of Li. When charged to 4.2 V, the decrease in the intensity of the 2100-ppm resonance and increase of the 750 ppm resonance indicates that Li ions in the TM layer are being pumped to the Na layer. When charged to 4.5 V, only 13.3% of total Li stays in the TM layer, while 80.9% Li now is stored in the Na layer. The good news is that these Li ions seem to get stuck in the Na layer and are not further extracted into the electrolyte, even at the high voltage of 4.5 V. This may be due to the formation of some stable local ordering, indicated by the newly appearing resonance at 500 ppm. On discharge, the Li ions in Na layer were pushed back into the TM layer by the repulsion of more and more inserting Na ions, as shown in Fig. 8f. The Li fate in the long-term cycling was summarized in Fig. 8g. After 40 cycles, Li in TM layer, which is the key stabilizer of the compound, decrease from 91% in the pristine to 49.2%; Li in Na layer, on the opposite, increase from 8.6% to 34.5%. More pronounced, the fraction of Li at surface in the Li-SEI-like phases increases to 4.4% and 16.3% after 10 and 40 cycles, respectively, which seems to be the major Li-loss mechanism. The total lithium amount by summing up all lithium environments, normalized with the mass of the samples, indicates that the total amount of lithium per formula unit decreases from 0.2 in pristine

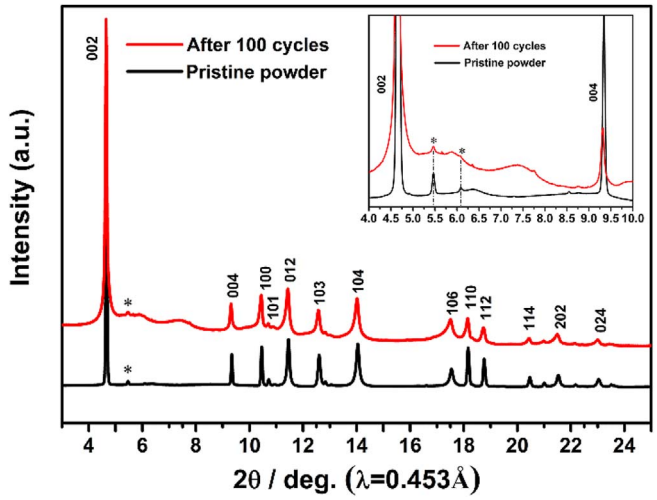

Fig. 7. SXRD patterns of a P2-$Na_{0.6}Li_{0.2}Mn_{0.8}O_2$ electrode mateials before and after long-tern cycles, including an extended view of the impurity and superlattice region (inset).

sample to 0.162 and 0.094 after 10 and 40 cycles, respectively. Apparently, some lithium in the pristine material is lost in the electrolyte or to the anode side, or, in the Li-SEI-like surface layer. The Li-loss and re-distribution may be one of the reasons for the capacity degradation of the electrode material.

4. Discussion

In this work, we designed and synthesized a group of lithium doped Mn-based P2 compounds $Na_xLi_yMn_{1-y}O_2$ as cathode materials for SIBs. All these materials exhibited very high initial capacities and many of them showed good capacity retention and high structural stability upon long-term cycling. Their performances are significantly superior to those of the undoped P2-Na_xMnO_2 materials [11,17,29] and some TM doped compounds, which suffered from the P2→O2 or P2→OP4 phase transitions induced by deintercalation of Na ions. In P2-Na_xMnO_2, the TM layer is fully occupied by +3 or +4 Mn during charging, therefore the oxygen atoms are apt to glide to accommodate the change of Mn-O bond length, causing the phase transitions [6]. In contrast, in doped P2-$Na_xLi_{1-y}Mn_yO_2$ materials, the Li-Mn clustering, evident from the

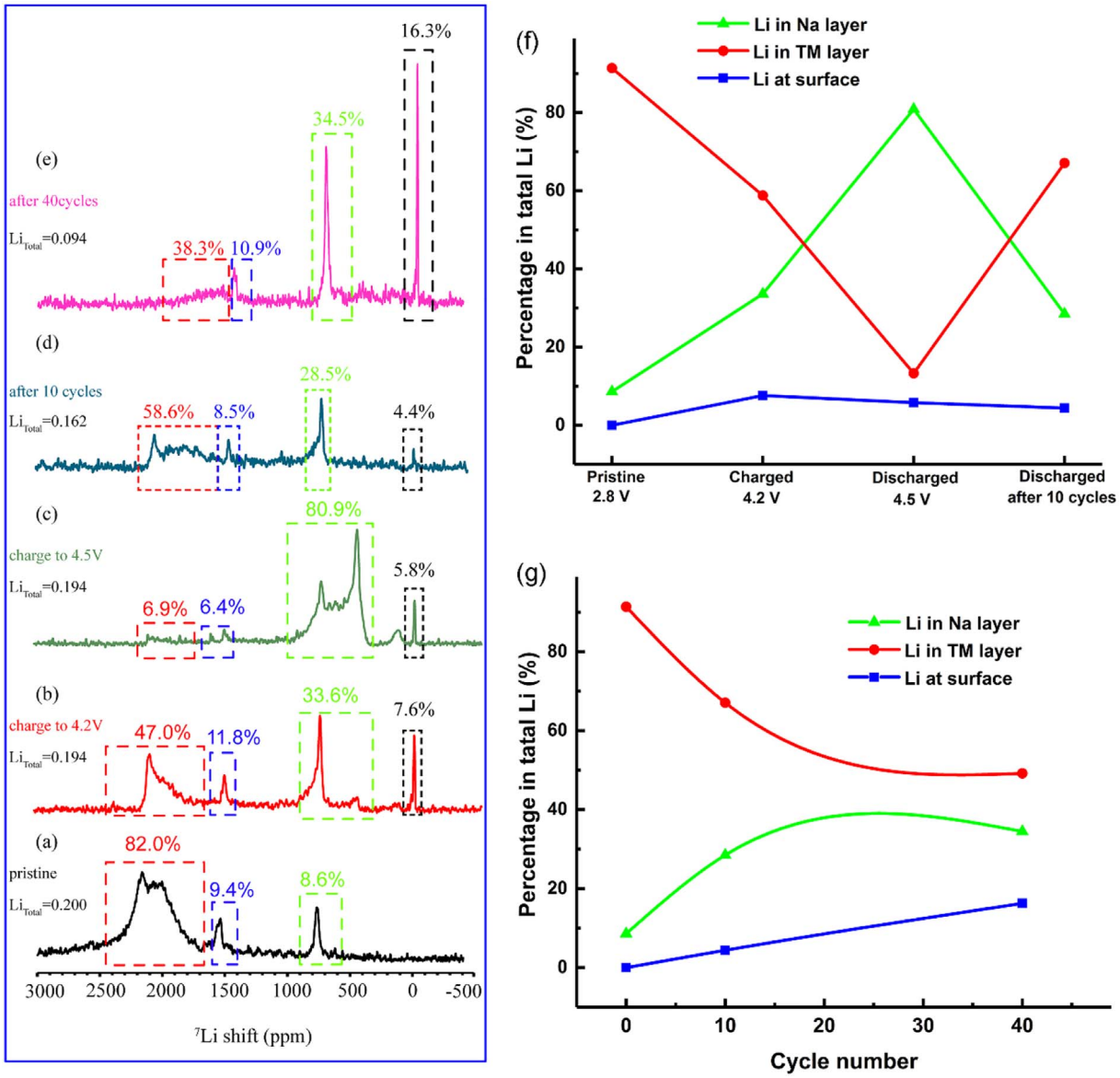

Fig. 8. ^{7}Li pjMATPASS NMR spectra of $Na_{0.6}Li_{0.2}Mn_{0.8}O_2$ electrode samples upon cycling: (a) pristine powder, (b) the electrode charged to 4.2 V; (c) 4.5 V, (d) discharged after 10 cycles and (e) discharged after 40 cycles. The amounts of Li at different sites in percentage of total Li in short term and in long term are summarized in (f) and (g), respectively.

superstructure peaks in XRD and similar to what is seen in Li rich cathode materials for LIBs and the solid state NMR results, together with the large ionic radius of Li^+ (0.76 Å) can effectively accommodate the Mn-O bond length change without initiating coordinated gliding of oxygen atoms. The undulated charge distribution (i.e. the Li^+ and Mn^{4+}) and the uneven bond lengths in the transition metal layer (i.e. Li-O and Mn-O bonds) makes the gliding of the O layer difficult. Such effects are commonly observed in many layered oxides. For example, $LiCoO_2$ undergoes a series of irreversible phase transitions from O3 to H1-3, then to O1 [46]. However, for $Li(NiCoMn)_{1/3}O_2$, it goes through a solid solution pathway, due to the undulated charge distribution of Ni^{2+} and Mn^{4+} [47]. NMR spectra further indicates that most Li in the TM layer exists in highly distorted octahedral sites. Such distorted octahedrons, to some extend like giant point defects, effectively pin the structure and make the coordinated gliding of oxygen atom throughout the crystal more difficult than the case where all bond lengths are similar, such as in $LiCoO_2$.

Accordingly, a single-phase, or solid solution-like phase evolution is observed within the P2 framework in these materials, as confirmed by the *in operando* XRD that covered quite a wide range of Na content (> 0.7 Na). The absence of gliding phase transition during cycling is believed to be the major contributing factor to both the high initial capacity and good capacity retention since dislocations and mechanical degradations induced by gliding phase transitions are largely avoided. Similar effects were also reported for Mg-doped manganese oxides. But the clustering effect of Li-Mn is much stronger than that of Mg-Mn. *Ex situ* SXRD on samples after 100 cycles and *in situ* SXRD on the long-term cycled samples, as seen in Fig. 7 and Fig. S6, respectively, further confirm the remarkable stability of the Li-doped P2 structure after extended cycling.

The absence of gliding phase transition also effectively reduces the strain associated with electrochemical cycling. The O2 or OP4 phase has significantly smaller unit cell volume than the P2 phase with similar Na-poor compositions. For instance, P2-type $Na_{0.67}Ni_{0.33}Mn_{0.67}O_2$ [30] and P2-$Na_{0.67}Fe_{0.5}Mn_{0.5}O_2$ [15] display a drastic shrinkage of the interlayer distance, leading to discharge capacity fade during cycles. While in P2-$Na_{0.6}Li_{0.2}Mn_{0.8}O_2$ material, the volume change between the end of charge and end of discharge was only about 3.7%, calculated form the *in situ* XRD patterns of the second cycle shown in Fig. S5. This volume change is extremely small, considering the relatively large radius of Na ions. The high capacity is also due partly to the contribution of reversible oxygen evolution, as shown in Fig. 3a (the CV curves), although its exact contribution to capacity is difficult to quantify because of the overlap with the contribution from electrolyte decomposition. The oxygen evolution includes irreversible oxygen loss in the forms of O_2 (or immediate reaction with electrolyte) and reversible oxidation/reduction through the formation of peroxide/superoxide-like O-O bonds [40,41]. The CV scans imply that the irreversible O_2 loss may gradually takes place in each cycle with a quickly diminished rate, while the reversible oxygen evolution is relatively stable in extended cycles. The accumulative loss of oxygen results in complicated compositional changes of the compound with the Mn: O ratio being increased from the pristine. For example, for a pristine composition of $Na_{0.6}(Li_{0.2}Mn_{0.8})O_2$, after many cycles, the composition that is actually reversibly cycling in the cell might be $Na_x(Li_{0.1}Mn_{0.9})O_2$, if assuming half of the Li is lost in the Li-SEI-like species, electrolyte or anode. This condensation effects of Mn also contributes to the fade of the reversible capacity. In addition, the oxygen evolution in layered oxide cathode materials is complicated and requires further investigation and understanding.

The use of Li as the dopant is highly effective in minimizing or eliminating phase transition during cycling. However, the optimal doping level still remains undetermined, as higher level Li doping lowers the theoretical capacity and drives the structure away from Na-P2, towards Li-Na-mixed O3, as shown in Fig. S3, and lower level Li doping, on the other hand, may not be sufficient to provide the local ordering to hinder the phase transitions. Fig. S8 compares the voltage profiles of four compositions in their second cycles. It can be seen that a slight change in Li doping level can results in significant change in the voltage hysteresis. Similar to what is reported in other compounds with reversible oxygen evolution, the voltage hysteresis (or, say, the overpotential) associated with Mn^{2+}/Mn^{3+} is relatively low and that associated with the oxygen revolution at high voltages is relatively high, which is unfavorable for energy storage efficiency.

Another important question is how to effectively keep as much as possible Li in the TM layer in extended cycling to retain their structural stabilization effect. Meng et al. [32] demonstrated that Li in TM layer can be extracted at high voltage and demonstrated this process is reversible in the first cycle. The results of our NMR experiments also suggest a high reversibility of this process, not only in the first cycle, but also in subsequent cycles. Furthermore the NMR data revealed the origin of this high reversibility. As shown in Fig. 8, upon charging, most Li ions are not extracted into the electrolyte. Instead, they migrate from the TM layer to the Na layer and are well kept there through the high voltage stage by the plausible stable local ordering. On discharge, the Li in the Na layer prefer to come back to the TM layers as large inter-slab spacing of the Na layer is unfavorable. This mechanism effectively keeps Li in the lattice of cathode and prevents significant Li-loss into the electrolyte from happening, which is the key reason for the good capacity retention in long term. The major Li-loss, however, is due to the formation of the Li-SEI-like phases at the surface. As indicated by the ^{7}Li solid-state NMR results, about half of the Li in the pristine sample is lost from the lattice of cathode and about half of Li in the TM layer is redistributed into the Li-SEI-like phases after 40 cycles. Interestingly, both the loss and distribution of Li seem to gradually reach equilibria in extended cycles, as demonstrated in Fig. 8g. This implies that it is possible to keep enough Li in the TM layer as the stabilizer and phase-transition preventer as designed in long term cycling. In situ XRD investigation on the long term cycled samples suggests that a small amount of Li remaining in the TM layer is still sufficient to help keeping the single-phase pathway even after 100 cycles. Strategies to more effectively reduce Li loss will be the key to further improve the capacity and retention of this class of compounds if thousands of cycles are targeted. On the other hand, the Li-loss mechanism might be different in the full cells. Works to address these questions are still on-going in our group.

5. Conclusion

A group of Li doped, Mn based intercalation compounds, with P2 structure and a formula of $Na_xLi_yMn_{1-y}O_2$, have been synthesized and systematically investigated to reveal the structure-property relationships. These compounds showed very high initial discharge capacity and outstanding capacity retention. It is rare to see such wide range of Na intercalation (~0.73 Na per formula unit) in the layered oxides with good reversibility. We believe that the absence of phase transition in these compounds during cycling, as revealed by *in operando* XRD, is primarily responsible for the excellent performance and the doping of Li in the TM layer is the key to induce and maintain such a single-phase evolution. The combination of *in operando* SXRD and SS-NMR reveals the critical role of lithium and its fate in extended cycling. The complicated electrochemical cycling process of this class of compounds, especially the processes associated with the oxygen evolution, remains to be explored. However, the excellent performance of these compounds open up new opportunities in the development of high capacity, long cycling life, and low cost sodium ion battery systems for large scale energy storage applications. The structural study provides new insights into rational design of Li-Na mixed layered oxides compounds, inspiring new strategies for designing high-performance intercalation cathode by tuning the composition and the crystal structure evolution in electrochemical cycling.

Acknowledgements

This work was supported by the U.S. National Science Foundation under grant numbers DMR-1410936, CBET-1706723 and DMR-1210792. The authors acknowledge Drs. Wenqian Xu, Jianming Bai and Eric Dooryhee for help in synchrotron data collection. H.C., X.M, S.X and L.Y. thank the financial supports from Georgia Tech new faculty startup fund. L.Y acknowledge a scholarship from the China Scholarship Council. Y.-Y. Hu and X. L. acknowledge support from the National Science Foundation under Grant No. DMR-1508404. All NMR experiments were carried out at the NHMFL supported by NSF under contract DMR-1157490. The use of the Advanced Photon Source and the National Synchrotron Light Source II were supported by the U.S. Department of Energy, Office of Science, through the general user programs.

Appendix A. Supplementary data

Supplementary data related to this article can be found at http://dx.doi.org/10.1016/j.jpowsour.2017.12.072.

References

[1] B. Dunn, H. Kamath, J.-M. Tarascon, Science 334 (2011) 928–935.
[2] N.S. Choi, Z. Chen, S.A. Freunberger, X. Ji, Y.K. Sun, K. Amine, G. Yushin, L.F. Nazar, J. Cho, P.G. Bruce, Angew. Chem. Int. Ed. 51 (2012) 9994–10024.
[3] D. Kundu, E. Talaie, V. Duffort, L.F. Nazar, Angew. Chem. Int. Ed. 54 (2015) 3431–3448.
[4] X. Xiang, K. Zhang, J. Chen, Adv. Mater. 27 (2015) 5343–5364.
[5] M.H. Han, E. Gonzalo, G. Singh, T. Rojo, Energy Environ. Sci. 8 (2015) 81–102.
[6] R.J. Clément, P.G. Bruce, C.P. Grey, J. Electrochem. Soc. 162 (2015) A2589–A2604.
[7] N. Ortiz-Vitoriano, N.E. Drewett, E. Gonzalo, T. Rojo, Energy Environ. Sci. 10 (2017) 1051–1074.
[8] C. Delmas, C. Fouassier, P. Hagenmuller, Physica B+ C 99 (1980) 81–85.
[9] X. Ma, H. Chen, G. Ceder, J. Electrochem. Soc. 158 (2011) A1307–A1312.
[10] J. Billaud, R.J. Clément, A.R. Armstrong, J. Canales-Vázquez, P. Rozier, C.P. Grey, P.G. Bruce, J. Am. Chem. Soc. 136 (2014) 17243–17248.
[11] A. Caballero, L. Hernan, J. Morales, L. Sanchez, J.S. Pena, M. Aranda, J. Mater. Chem. 12 (2002) 1142–1147.
[12] R. Berthelot, D. Carlier, C. Delmas, Nat. Mater. 10 (2011) 74–80.
[13] M. Guignard, C. Didier, J. Darriet, P. Bordet, E. Elkaïm, C. Delmas, Nat. Mater. 12 (2013) 74–80.
[14] X. Li, X. Ma, D. Su, L. Liu, R. Chisnell, S.P. Ong, H. Chen, A. Toumar, J.-C. Idrobo, Y. Lei, Nat. Mater. 13 (2014) 586–592.
[15] N. Yabuuchi, M. Kajiyama, J. Iwatate, H. Nishikawa, S. Hitomi, R. Okuyama, R. Usui, Y. Yamada, S. Komaba, Nat. Mater. 11 (2012) 512–517.
[16] L. Liu, X. Li, S.H. Bo, Y. Wang, H. Chen, N. Twu, D. Wu, G. Ceder, Adv. Eng. Mater. 5 (2015) 1500944.
[17] X. Wang, M. Tamaru, M. Okubo, A. Yamada, J. Phys. Colloid Chem. 117 (2013) 15545–15551.
[18] B.M. de Boisse, D. Carlier, M. Guignard, L. Bourgeois, C. Delmas, Inorg. Chem. 53 (2014) 11197–11205.
[19] E. Talaie, V. Duffort, H.L. Smith, B. Fultz, L.F. Nazar, Energy Environ. Sci. 8 (2015) 2512–2523.
[20] J. Wang, X. He, D. Zhou, F. Schappacher, X. Zhang, H. Liu, M.C. Stan, X. Cao, R. Kloepsch, M.S. Sofy, G. Schumacher, J. Li, J. Mater. Chem. A 4 (2016) 3431–3437.
[21] M.H. Han, E. Gonzalo, N. Sharma, J.M. López del Amo, M. Armand, M. Avdeev, J.J. Saiz Garitaonandia, T. Rojo, Chem. Mater. 28 (2016) 106–116.
[22] X. Wu, J. Guo, D. Wang, G. Zhong, M.J. McDonald, Y. Yang, J. Power Sources 281 (2015) 18–26.
[23] X. Li, D. Wu, Y.-N. Zhou, L. Liu, X.-Q. Yang, G. Ceder, Electrochem. Commun. 49 (2014) 51–54.
[24] C. Ma, J. Alvarado, J. Xu, R.J. Clément, M. Kodur, W. Tong, C.P. Grey, Y.S. Meng, J. Am. Chem. Soc. 139 (2017) 4835–4845.
[25] E. de la Llave, E. Talaie, E. Levi, P.K. Nayak, M. Dixit, P.T. Rao, P. Hartmann, F. Chesneau, D.T. Major, M. Greenstein, Chem. Mater. 28 (2016) 9064–9076.
[26] N. Yabuuchi, R. Hara, M. Kajiyama, K. Kubota, T. Ishigaki, A. Hoshikawa, S. Komaba, Adv. Eng. Mater. 4 (2014) 1301453.
[27] D. Kim, S.H. Kang, M. Slater, S. Rood, J.T. Vaughey, N. Karan, M. Balasubramanian, C.S. Johnson, Adv. Eng. Mater. 1 (2011) 333–336.
[28] N.K. Karan, M.D. Slater, F. Dogan, D. Kim, C.S. Johnson, M. Balasubramanian, J. Electrochem. Soc. 161 (2014) A1107–A1115.
[29] J. Billaud, G. Singh, A.R. Armstrong, E. Gonzalo, V. Roddatis, M. Armand, T. Rojo, P.G. Bruce, Energy Environ. Sci. 7 (2014) 1387–1391.
[30] D.H. Lee, J. Xu, Y.S. Meng, Phys. Chem. Chem. Phys. 15 (2013) 3304–3312.
[31] P.F. Wang, Y. You, Y.X. Yin, Y.S. Wang, L.J. Wan, L. Gu, Y.G. Guo, Angew. Chem. Int. Ed. 55 (2016) 7445–7449.
[32] J. Xu, D.H. Lee, R.l.J. Clément, X. Yu, M. Leskes, A.J. Pell, G. Pintacuda, X.-Q. Yang, C.P. Grey, Y.S. Meng, Chem. Mater. 26 (2014) 1260–1269.
[33] E. de la Llave, E. Talaie, E. Levi, P.K. Nayak, M. Dixit, P.T. Rao, P. Hartmann, F. Chesneau, D.T. Major, M. Greenstein, Chem. Mater. 28 (2016) 9064–9076.
[34] N. Yabuuchi, K. Yoshii, S.-T. Myung, I. Nakai, S. Komaba, J. Am. Chem. Soc. 133 (2011) 4404–4419.
[35] A.C. Larson, R.B. Von Dreele, General Structure Analysis System, LANSCE, MS-H805, Los Alamos, New Mexico, 1994.
[36] B.H. Toby, J. Appl. Crystallogr. 34 (2001) 210–213.
[37] J. Wang, X. He, E. Paillard, N. Laszczynski, J. Li, S. Passerini, Adv. Eng. Mater. 6 (2016) 1600906.
[38] N. Yabuuchi, R. Hara, K. Kubota, J. Paulsen, S. Kumakura, S. Komaba, J. Mater. Chem. 2 (2014) 16851–16855.
[39] H. Chen, M.S. Islam, Chem. Mater. 28 (2016) 6656–6663.
[40] K. Luo, M.R. Roberts, R. Hao, N. Guerrini, D.M. Pickup, Y.-S. Liu, K. Edström, J. Guo, A.V. Chadwick, L.C. Duda, Nat. Chem. 8 (2016) 684–691.
[41] H. Koga, L. Croguennec, M. Ménétrier, P. Mannessiez, F. Weill, C. Delmas, S. Belin, J. Phys. Colloid Chem. 118 (2014) 5700–5709.
[42] I. Hasa, D. Buchholz, S. Passerini, B. Scrosati, J. Hassoun, Adv. Eng. Mater. 4 (2014) 1400083.
[43] C.P. Grey, N. Dupré, Chem. Rev. 104 (2004) 4493–4512.
[44] Y.J. Lee, F. Wang, C.P. Grey, J. Am. Chem. Soc. 120 (1998) 12601–12613.
[45] W. Bowden, T. Bofinger, F. Zhang, N. Iltchev, R. Sirotina, Y. Paik, H. Chen, C. Grey, S. Hackney, New manganese dioxides for lithium batteries, J. Power Sources 165 (2) (2007) 609–615 https://doi.org/10.1016/j.jpowsour.2006.10.041.
[46] A. Van der Ven, M.K. Aydinol, G. Ceder, Phys. Rev. B 58 (1998) 2975–2987.
[47] W.S. Yoon, K.Y. Chung, J. McBreen, X.Q. Yang, Electrochem. Commun. 8 (2006) 1257–1262.